THE EFFECTS OF INTERSTITIAL FLUID FLOW ON THE RESPONSE OF SOFT TISSUE STRAIN AND THE FEASIBILITY OF POROELASTICITY IMAGING

Ricardo Leiderman, leider@mecanica.ufrj.br
Programa de Engenharia Mecanica, COPPE-UFRJ, Ilha do Fundão.

Paul E. Barbone, barbone@bu.edu
Department of Aerospace and Mechanical Engineering, Boston University, Boston, MA 02215.

Assad A. Oberai, oberaa@rpi.edu
Department of Mechanical, Aerospace and Nuclear Engineering, Rensselaer Politechnic Institute, Troy, NY 12180.

Jeffrey C. Bamber, jeff@icr.ac.uk
Physics Department, Institute of Cancer Research, United Kingdom.

Abstract. *In the present work we investigate the effects of interstitial fuid flow and interstitial fluid drainage on the spatio-temporal response of soft tissue strain. Our motivation comes from the ability to measure in vivo strain distributions in soft tissue via elastography, and the possibility of using such techniques to investigate soft tissue fluid flow. Our study is based upon a mathematical model for soft tissue mechanics from the literature. It is a simple generalization of biphasic theory that includes not only the coupling between the tissue fluid and solid phases, but also the fluid exchange between the interstitium and the local microvasculature. As in the biphasic theory, it follows from the assumption that both solid and fluid phases are incompressible that dilatation can occour only when the corresponding volume of fluid percolates or drains from the interstitial compartment. We solve the mathematical equations in two dimensions by the finite element method (FEM). Realistic input tissue properties from the literature are used in conjunction with FEM modelling to conduct several computational experiments relevant to quasistatic imaging for the characterization of fluid flow in solid tumors. The results of these simulations lead to the following conclusions: (i) different hypothetical flow mechanisms lead to different spatio-temporal patterns of stress/strain relaxation; (ii) representative tissue properties show fluid drainage into the local microvasculature to be the dominant flow-related stress/strain relaxation mechanism; (iii) the relaxation time of solid tumours due to fluid drainage into the microvasculature is on the order of 5 - 10 s; (iv) under realistic applied pressure magnitudes, the magnitude of the strain relaxation can be as high as approximately 0.4% strain (4000 microstrains), which is well within the range of strains measurable by elastography.*

Keywords*: soft tissue relaxation, interstitial fluid flow, poroelasticity, elastography*

1. INTRODUCTION

Elastography refers to a collection of imaging techniques that allow mechanical strain distributions to be imaged and noninvasively quantified *in vivo*.

Soft tissue is widely recognized as having both fluid and solid phases which can move independently of each other. Furthermore, the fluid exists within several ``compartments" of the soft tissue, notably, the vasculature (including both the hemal and lymphatic vessels) and the extravascular space. Of course, due to the hydraulic conductivity of the microvessel walls in both vascular networks, fluid is often exchanged between these compartments. It is recognized that fluid flow leads to a stress relaxation at fixed strain (or conversely, a strain relaxation at fixed stress). It is reasonable to conjecture then, that by measuring the spatio-temporal patterns of strain in a strain-relaxation type of experiment, the effects of fluid flow can be visualized and measured.

The linear ``biphasic theory" (Mow *et al*., (1980)), which can be regarded as a special case of Biot poroelasticity; the special case being that of having two incompressible phases, has been very successful at modeling the fluid-elastic coupling in cartilage. Cartilage tends to be avascular, however, and so fluid resides only in the ``extravascular compartment".

A different model for the mechanics of vascularized soft tissue, which includes the effects of fluid flow and the possibility of exchange between fluid compartments was proposed by R. Skalak, RK Jain, and coworkers in Netti *et al*. (1997). The model was originally developed in a rather general context to capture effects of fluid-elastic coupling in soft tissues, but was then applied to describe perfusion and drug delivery in solid tumors.

Our motivation for this work stems from the question: Can techniques from elastography be used to image and quantify interstitial fluid flow in soft tissues from spatio-temporal patterns of elastic strain? To answer this, we use the mathematical model of Netti *et al*. (1997) in conjunction with finite element modeling to predict the effects of fluid

flow on the spatio-temporal patterns of soft-tissue elastic strain under a variety of physiological conditions. The magnitude of the strain effects and their time scales dictate the measurability of the effects of fluid flow.

Simulations relevant to a quasistatic elasticity imaging for the characterization of fluid flow in solid tumors are emphasized here. In particular, we show that solid tumors tend to relax much faster than healthy tissue due to its high filtration coefficient (angiogenesis), which is recognized to be one of the most important features of tumors regarding diagnostics and prognostics.

In the following section, we describe the used mathematical model. We then describe two computational simulations designed to investigate the question raised above. This is followed by Discussion and Conclusions.

2. MATHEMATICAL MODEL

A complete derivation of the mathematical model can be found in Netti *et al*. (1997) and in Leiderman *et al*. (2006). A summary is given in the following. Figure 1 represents schematically a portion of soft tissue. Its boundary and domain are denoted by Γ and Ω, respectively. The interstitial boundary, Γ, is comprised of three parts: the outer boundary Γ_o, the interface with the hemal capillaries Γ_c, and the interface with the lymphatic capillaries Γ_L. Due to the hydraulic conductivity of the microvessel walls, fluid is often exchanged at Γ_c and Γ_L. This fluid exchange is governed by the Starling's law, which states that the flaw rate across a membrane (the capillary wall in the present case) is proportional to the pressure jump across the membrane. We regard the interstitial compartment as a linear biphasic solid-fluid mixture, where both fluid and solid phases can move independently of each other. The two phases are treated as intrinsically incompressible.

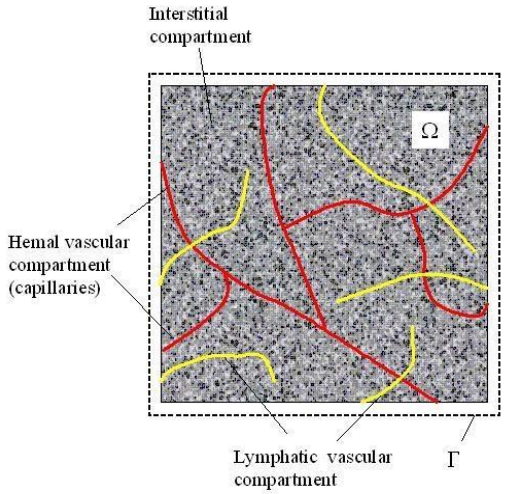

Figure 1: A portion of soft tissue: The interstitial compartment is itself a biphasic solid-fluid mixture, where both fluid and solid phases can move independently of each other.

The assumptions that go into the model are linear isotropic constitutive equations, small strains, small vascular space, Starling's law for (transient) fluid transport across the vessel wall, Darcy's law for fluid flow through the interstitial compartment, and Hooke's law for the elastic response. We further assume the deformation takes place slowly enough that inertia can be neglected. Under these conditions, the solid displacement vector **u** and interstitial fluid pressure p are related by:

$$\nabla \cdot \dot{\mathbf{u}} - \nabla[\kappa \nabla p] + \chi p = 0 \tag{1}$$

$$\nabla \cdot [-p\mathbf{I} + \lambda \nabla \cdot \mathbf{u}\mathbf{I} + \mu(\nabla \mathbf{u} + (\nabla \mathbf{u})^T)] = 0 \tag{2}$$

Equation (1) represents a combination of the conservation of fluid mass in the interstitium, with the momentum equation for the fluid phase. Equation (2) represents the balance of total linear momentum in the tissue. The equations above describe a *homogenized* medium in which each elementary continuum element contains a large number of microvessels. Therefore, we expect the model to work well at scales of $O(1\text{mm}^3)$, but not down to scales of $O(1\mu\text{m}^3)$. The symbols that appear in Equations (1) and (2) are defined as follows: ∇ is the gradient operator; **I** is the identity tensor; $\dot{\mathbf{u}}$ is the solid phase velocity; κ is the interstitial permeability associated to the Darcy's law that governs the ease by which fluid percolates through the interstitium; λ and μ are the elastic Lamé parameters of the drained

interstitium (also called the solid matrix bellow); and χ is the average filtration coefficient associated to the Starling's law, given by:

$$\chi = \chi_V + \chi_L, \tag{3}$$

where

$$\chi_V = \frac{L_P S_V}{V} \; ; \; \chi_L = \frac{L_{PL} S_L}{V}. \tag{4}$$

Here, L_P (resp. L_{PL}) is the hydraulic conductivity of the hemal (resp. lymphatic) capillary wall and $\frac{S_V}{V}$ (resp. $\frac{S_L}{V}$) is the surface area of the hemal (resp. lymphatic) capillary wall per unit volume of tissue.

In the special case $\chi = 0$, we recover the linear biphasic equations describing the deformation of avascular cartilage like materials. It's implicit in the Equations (1) and (2) that the vascular pressure relaxes much faster than the interstitial pressure (fluid can redistribute much faster within the vascular compartment than within the interstitium). In that sense, the pressure p that appears in the equations is actually the fluctuating part of the interstitial pressure.

It is implicit in the model that, in general, mechanical loading not only strains the tissue, but also pressurizes both solid and fluid phases. The pressurization mechanism can be understood based on the mechanical behavior of the drained interstitium (elastic solid matrix). In contrast to the solid phase, the solid matrix is compressible, i.e., it reduces its volume when a mechanical loading is applied by reducing its pore space volume. In an ideal case, where there is no saturating fluid or the saturating fluid can move frictionless within the pore system and drain freely to the vascular compartment, the pore system would shrink instantaneously in response to the applied loading. However, as the interstitial fluid face resistance to percolate and drain, it resists to the pore system shrinking, pressurizing and being pressurized by the solid phase. Relaxation takes place, i.e., pressure drops gradually, as the interstitial fluid percolates or drains in response to the pressurization. During the relaxation the tissue approaches to the solid matrix static equilibrium. At static equilibrium, $p=0$, and the mechanical behavior is governed by the solid matrix Lamé parameters. It follows from the assumption that both solid and fluid phases are incompressible that infinitesimal dilatation can occur only when the corresponding volume of fluid percolates or drains to vascular or lymphatic systems.

3. SIMULATIONS

In order to evaluate the predictions of the mathematical model with nontrivial geometries and boundary conditions, we developed a finite element discretization of Equations (1) and (2) in two dimensions. We used the standard Galerkin approximation with bilinear shape functions for both the pressure and displacement fields. To integrate in time we use the Backward Euler method, assuming all material parameters are constant with time. We have validated our implementation by comparing the numerical solution to the analytical solution derived in Leiderman et al. (2006).

We now use this finite element implementation to study problems that model hypothetical clinical imaging exams. In the computational experiments presented here, we tried to reproduce two hypothetical configurations for clinical breast exams, and investigate the strain relaxation within the sample. For both simulations we used bilinear finite elements on a 1000 x 1000 mesh, and backward Euler time marching with a time step of 0.03 s.

The poroelastic medium is defined by 4 physical parameters: λ, μ, κ and χ. In what follows, we work in plane strain state. The 2-D scenario assumed in the computational simulations is that of a circular inclusion embedded in a square tissue sample, as shown in Figs. 2 and 4. The circular inclusion is intended to represent a malignant breast tumor, with stiffness, microvessel density, hydraulic conductivity, and connective tissue permeability all elevated relative to the background, normal, values.

The tissue surrounding the inclusion is assumed to have ``normal'' biomechanical properties. The shear modulus, μ, was chosen according the values reported for breast tissue in Sarvazyan (2001) assuming that it is the same for the saturated poroelastic (incompressible) medium and the corresponding solid matrix. We then calculated the corresponding value for λ assuming a Poisson ratio of 0.49. The values for κ and χ were chosen according to values given in Netti *et al*. (1995).

Regarding the inclusion, in order to reproduce a solid tumor behavior, we assumed an augmented capillary filtration coefficient in all the experiments. We also assumed it is stiffer, increasing the value of μ, and assumed a Poisson ratio of *0.47*, calculating λ accordingly. All the parameters used are summarized in Table I.

Table I: Poroelastic parameters used in simulations

Parameter	Healthy tissue	Tumor
χ (Pa.sec)$^{-1}$	1.89×10^{-8}	5.67×10^{-7}
κ (m^2/(Pa.sec))	6.4×10^{-15}	3.1×10^{-14}
λ (kPa)	539	517
μ (kPa)	11	33

3.1. Simulation 1

Experiment 1 is schematically shown in Fig.2. The circular inclusion has *1cm* diameter and the sample has dimensions *10cm x 10cm*. The fluid *cannot* flow across the boundaries, mimicking a portion of tissue *completely* bounded by skin. Therefore, the interstitial fluid can redistribute, but the only way for it to leave the sample is by vascular drainage. Such an idealized boundary condition is valid when the drainage effects are much larger than the percolation effects and the permeable boundary is relatively far away from the region to be investigated, as in the case here. The tissue is fixed at the bottom, where $u_x=u_y=0$. The lateral surfaces are traction free. At the top, we simulate the mechanical loading from a compressor of *5cm* of width. The displacement of the compressor is modeled by a ramp function such that the prescribed u_y goes from *0* to *1cm* in *0.3sec*, in the region corresponding to *x=2.5cm* to *x=7.5cm*. Below the compressor we prescribe zero shear stress, which models a slip boundary condition.

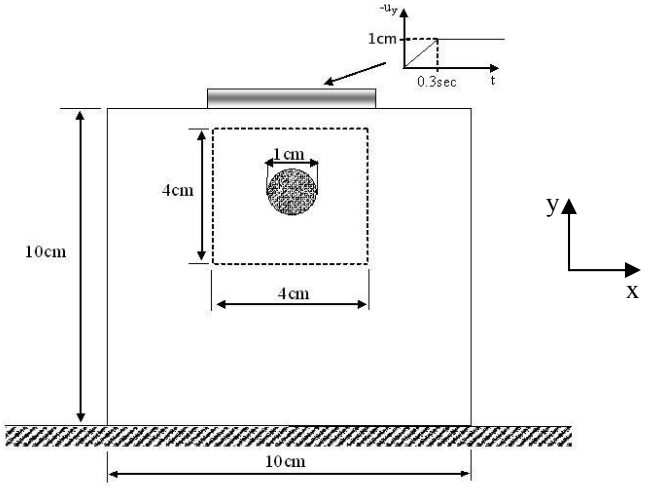

Figure 2: Experiment 1. The circular inclusion has *1cm* diameter and the sample has dimensions *10cm* x *10cm*. At the top, we simulate the mechanical loading from a compression of *5cm* of width.

In Fig.3 we show results corresponding to the region delimited by the dotted line in Fig.2. It has dimensions of *4cm* x *4cm* and is contained between *x=3.0cm* to *x=7.0cm* and *y=5.5cm* to *y=9.5cm*. We emphasize that we have solved the problem in the entire domain, but are showing the results only in this region of interest, in order to investigate the behavior of the inclusion and its surroundings in detail. This is intended to be representative of ultrasound imaging where the physical boundaries are typically distinct from the image boundaries.

In this experiment, the fluid exchange between interstitial and microvascular compartments is the dominant phenomenon. Due to the difference between the filtration coefficient inside and outside the inclusion (it is 30 times larger inside), a transient analysis of the problem can be outlined considering two different time scales: the inclusion's relatively short relaxation time and the surrounding tissue's large relaxation time.

Right after the mechanical loading has been applied and before significant fluid drainage has occurred, the tissue is pressurized and the sample approximately behaves like an incompressible elastic solid, with the same shear modulus (μ) as the corresponding solid matrix and a Young's modulus equals to 3μ. The pressure (kPa) field at *t=0.3sec* is shown in Fig. 3(a). We can see the stress concentrations at the transducer edges radiating in the upper left and right corners of the figure. At the center, we can distinguish the inclusion and four lobes resulting from the stress concentration at the inclusion.

Gradually, as the fluid drains from the interstitium to the microvasculature, the tissue relaxes. In Fig. 3(b) we plot the pressure (kPa) field at *t=5.4sec*. The comparison between Figs. 3(a) and 3(b) shows that the inclusion relaxes much faster than the surrounding tissue. This may be attributed to the higher value of the microvascular filtration coefficient in the inclusion. In Fig. 3(c) we plot the difference in the *x*-normal strain field (ε_{xx}) between *t= 0.3sec* and *t= 5.4sec*,

i.e., $\varepsilon_{xx}(t=5.4sec)$ - ε_{xx} $(t=0.3sec)$. In Fig. 3(d) we plot $\varepsilon_{yy}(t=5.4sec)$ - $\varepsilon_{yy}(t=0.3sec)$ and in Fig. 3(e) we plot the corresponding dilatation difference, i.e., $(\varepsilon_{xx}(t=5.4sec) + \varepsilon_{yy}(t=5.4sec)) - (\varepsilon_{xx}(t=0.3sec) + \varepsilon_{yy}(t=0.3sec)) = \Delta(t=5.4sec) - \Delta(t=0.3sec)$. We observe that the dilatation in the inclusion is negative, indicating that it is shrinking as it relaxes. On the other hand, the volume of the surrounding tissue remains almost unchanged ($\Delta \approx 0$). We also observe four lobes in Figs 3(c) and 3(d) resulting from the stress concentration redistribution around the inclusion, which has occurred during the relaxation. We can see in Fig. 3(e) that the fluid drainage at the lobes is small, since the dilatation in this region is almost zero. In summary, at *t=5.4sec*, the mechanical behavior of the inclusion is approximately governed by the corresponding solid matrix mechanical properties; that is, it has relaxed, while the surrounding tissue still behaves like an incompressible material.

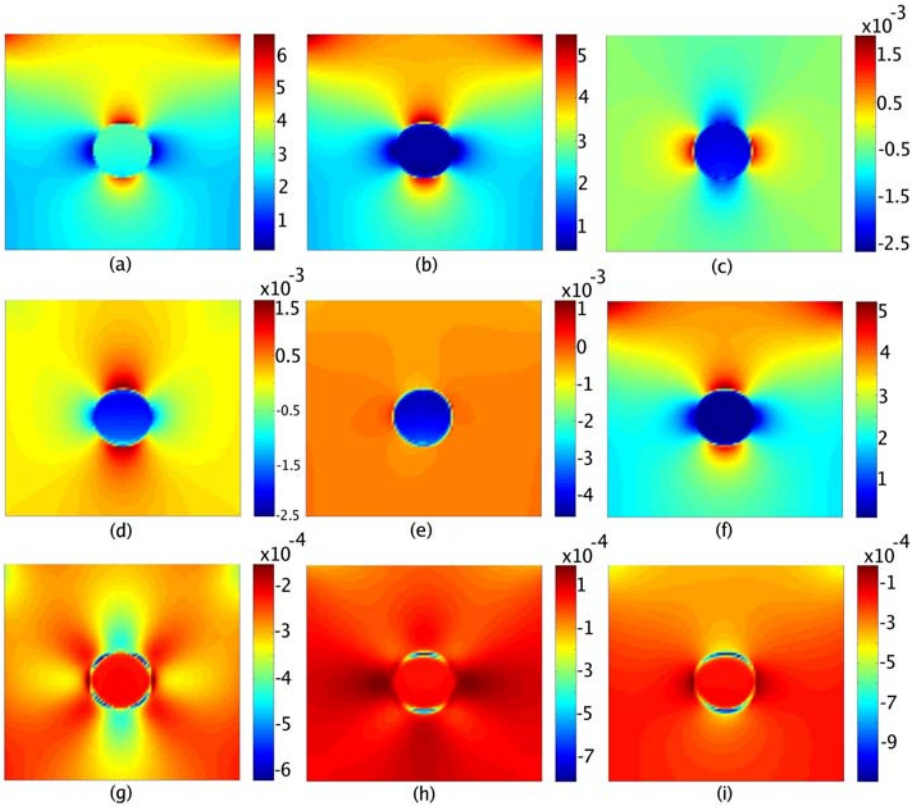

Figure 3: (a) The pressure field (kPa) at *t=0.3sec*. (b) The pressure field (kPa) at *t=5.4sec*. (c) ε_{xx}(t=5.4sec) - ε_{xx} (t=0.3sec). (d) ε_{yy}(t=5.4sec) - ε_{yy} (t=0.3sec). (e) Δ(t=5.4sec) - Δ(t=0.3sec). (f) The pressure field (kPa) at *t=10.2sec*. (g) ε_{xx} (t=15.0sec)} - ε_{xx} (t=10.2sec). (h) ε_{yy} (t=15.0sec)} - ε_{yy} (t=10.2sec). (i) Δ (t=15.0sec) - Δ (t=10.2sec).

The inclusion takes about *10secs* to relax almost completely. In the Fig. 3(f) we plot the pressure (kPa) field at *t=10.2sec*. We observe that the pressure inside the inclusion is close to the equilibrium pressure ($p \approx 0$). In Fig. 3(g) we plot $\varepsilon_{xx}(t=15sec)$ - $\varepsilon_{xx}(t=10.2sec)$, in Fig. 3(h) we plot $\varepsilon_{yy}(t=15sec)$ - $\varepsilon_{yy}(t=10.2sec)$ and in Fig. 3(i) we plot $\Delta(t=15sec)$ - $\Delta(t=10.2sec)$. Now, both the inclusion and the surrounding tissue relax by similar small amounts. Due to the applied displacement, we see that the strain occurs predominantly in the *x* direction and both inclusion and surrounding tissue shrink at approximately the same rate. We also observe that the interstitial fluid drains faster (or percolates) in a thin region around the inclusion, due to the stress concentration. The surrounding tissue takes about *300sec* to relax almost completely. As discussed before, at the steady state, where both inclusion and surrounding tissue are relaxed, the sample assumes the configuration where the mechanical behavior of both inclusion and surrounding tissue are governed by the respective solid matrix Lamé parameters.

3.2. Simulation 2

Experiment 2 is schematically shown in Fig. 4. The circular inclusion still has *1cm* diameter, while the model still has dimensions of *10cm* x *10cm*. As before, the fluid cannot flow across the boundaries and the tissue is fixed at the bottom. However, now the model is completely confined at the top, where u_y goes from *0* to *0.03cm* in *0.3sec*, and is partially confined at the lateral surfaces, i.e., $u_x=0$ from *y=2.0cm* to *y=10cm*, while it is traction free from *y=0.0cm* to

y=2.0cm. The goal here is to reproduce a situation of partial breast confinement, with the recognition that the breast cannot be completely confined in the clinic.

Here, as before, the fluid exchange between interstitial and microvascular compartments is the dominant phenomenon. A transient analysis of the problem can again be outlined by considering two different time scales. The pressure (kPa) field at *t=0.3sec* is shown in Fig. 5(a). We see that the pressure magnitude is similar to the previous case despite the much smaller displacement prescribed at the top boundary. This is obtained by confining a portion of the lateral surface. We also observe that in contrast to the previous case, there is no stress concentration in the upper left and right corners and the pressure field is almost uniform.

As the interstitial fluid drains, the inclusion relaxes. The pressure (kPa) field at *t=6.3sec* is shown in Fig. 5(b). We can see that the pressure inside the inclusion is about *85%* smaller at *t=6.3sec* than at *t=0.3sec*, while it remains close to the peak in the surrounding tissue. Once again this is due to the higher vascular filtration in the inclusion. In the Fig. 5(c) we plot $\varepsilon_{xx}(t=6.3sec) - \varepsilon_{xx}(t=0.3sec)$, in Fig. 5(d) we plot $\varepsilon_{yy}(t=6.3sec) - \varepsilon_{yy}(t=0.3sec)$ and in Fig. 5(e) we plot $\Delta(t=6.3sec) - \Delta(t=0.3sec)$. As in the previous case, we observe that the dilatation in the inclusion is negative, indicating that it is shrinking as it relaxes, and the volume of the surrounding tissue remains almost unchanged ($\Delta \approx 0$). We also see four lobes resulting from the stress concentration redistribution around the inclusion.

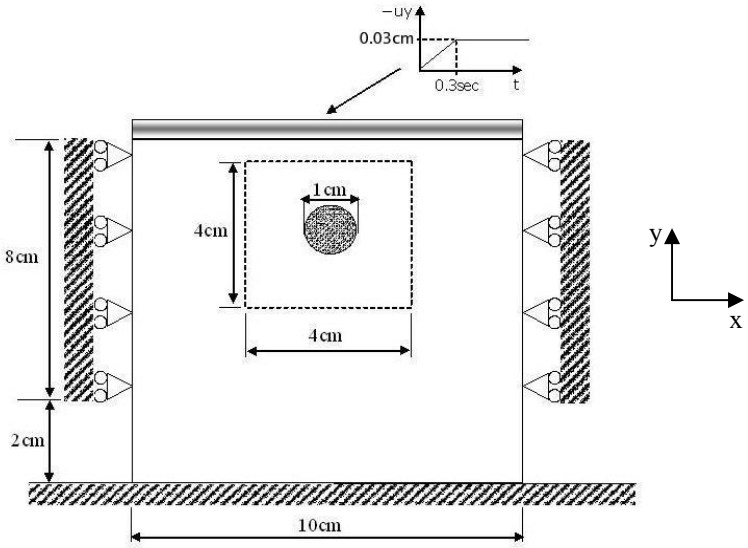

Figure 4: Experiment 2: The circular inclusion has *1cm* diameter and the sample has dimensions of *10cm* x *10cm*. The model is completely confined at the top, where u_y goes from *0* to *0.03cm* in 0.3sec, and is partially confined on the sides from *y=2.0cm* to *y=10cm*. The goal is to reproduce a situation of partial confined test.

The inclusion takes about *10sec* to relax almost completely. The pressure (kPa) field for *t=13.5sec* is shown in Fig. 5(f). The pressure inside the inclusion is now negative, indicating that fluid is draining back to the interstitial compartment from the microvasculature, as the surrounding tissue relaxes. In Fig. 5(g) we plot $\varepsilon_{xx}(t=31.5sec) - \varepsilon_{xx}(t=13.5sec)$, in Fig. 5(h) we plot $\varepsilon_{yy}(t=31.5sec) - \varepsilon_{yy}(t=13.5sec)$ and in Fig. 5(i) we plot $\Delta(t=31.5sec) - \Delta(t=13.5sec)$. In contrast to the previous case, due to the boundary conditions, the strain predominantly occurs in the *y* direction. Further, in agreement with the pressure field shown in the Fig.5(f), we observe that during this period the inclusion swells while the surrounding tissue shrinks. In fact, the inclusion attains its smallest volume at approximately *t=13sec* then swells till the sample reaches the steady state configuration.

4. DISCUSSION

In Experiment 1, we observe that in the first 5 seconds the inclusion relaxes much more than the surrounding tissue. During this time, its volume reduces by about *4,000* microstrains. For an inclusion of *1cm* diameter this implies displacements of the order of *40*μm. On the other hand, after the inclusion stops relaxing, the surrounding tissue relaxation becomes the predominant phenomenon. Since drainage is the main relaxation mechanism for both inclusion and surrounding, their relaxation time scales are directly proportional to the respective filtration coefficient values and, can be roughly estimated by $\frac{1}{\chi(\lambda+2\mu)}$. In terms of the shrinking magnitude resulting from the relaxation, it is directly proportional to the applied displacement at the boundary. Further, it is also directly proportional to the Poisson's

ratio difference between incompressible material (*0.5*) and the solid matrix, i.e., the smaller the solid matrix Poisson's ratio, the larger the shrinking.

As in the previous experiment, we see in Experiment 2 that in the first 6 seconds the inclusion shrinks about *4,000* microstrains, which, again, for an inclusion of *1cm* diameter implies displacements of the order of *40*μ. The applied displacement, the unconfined to confined lateral area ratio and the inclusion solid matrix *bulk modulus* determine the shrinking magnitude. In the limit case, where the sample is completely confined, practically all the sample's volume reduction resulting from the applied displacement must be reflected in the inclusion's volume reduction. We observed also that after the inclusion relaxes it experiences a gradual swelling, while the surrounding relaxation takes place. It can be understood by recognizing that the surrounding tissue shrinks as it relaxes, because its solid matrix is compressible. The shrinking is partially balanced by the inclusion's swelling. Again, in the limit case, where the sample is completely confined all the shrinking must be balanced by the inclusion's swelling.

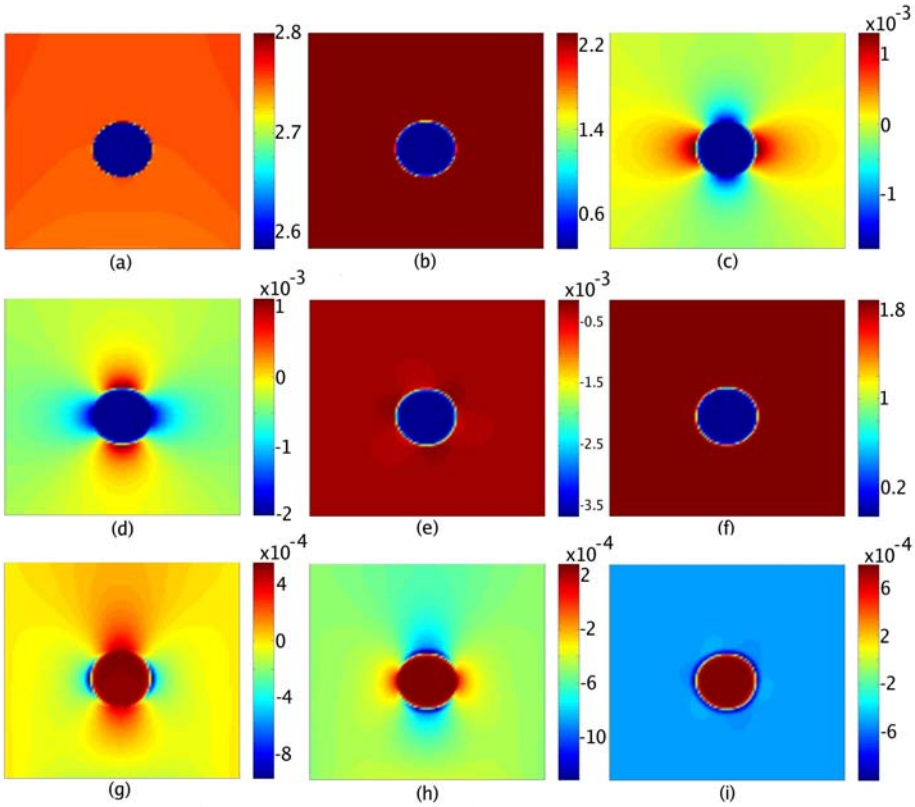

Figure 5: (a) The pressure field (kPa) at *t=0.3sec*. (b) The pressure field (kPa) at *t=6.3sec*. (c) ε_{xx}(*t=6.3sec*) - ε_{xx} (*t=0.3sec*). (d) ε_{yy}(*t=6.3sec*) - ε_{yy} *(t=0.3sec*). (e) Δ(*t=6.3sec*) - Δ(*t=0.3sec*). (f) The pressure field (kPa) at *t=13.5sec*. (g) ε_{xx} (*t=31.5sec*)} - ε_{xx} (*t=13.5sec*). (h) ε_{yy} (*t=31.5sec*) - ε_{yy} (*t=13.5sec*). (i) Δ(*t=31.5sec*) - Δ(*t=13.5sec*).

The results suggest that it may be possible to image the interstitial fluid motion in tissues by measuring the corresponding strain rate. A sequence of images acquired from ultrasound or other scanners could be processed, as they are in elasticity imaging, to track the spatio-temporal patterns of elastic strain. In addition, the strain pattern could then be used to solve for the spatial distribution of the poroelastic parameters, in particular, the shear modulus μ and the microvascular filtration coefficient χ.

It is interesting to consider the ultrasound measurability of the transient strains predicted here. In experiment 1, we noted a volume change in the inclusion of about *0.4%* after 5 seconds, in an overall compression of *10%*. Such a relaxation would certainly be measurable by ultrasound, though tracking a compression over a full *10%* strain might present technical difficulties. On the other hand, in experiment 2, with confined compression of *0.3%* we noted the same inclusion volume change of *0.4%* over about 6 seconds. The volume change is roughly isotropic in the plane, so about half that of that, or about *0.2%*, would take place in the high resolution (ultrasound propagation) direction. In practice, it's likely that the plane strain assumption would be violated here, and the volume change might be expected to be isotropic in the volume. In that case, only about *1/3* of the total volume change, or about *0.15%* strain, would be reflected in the high resolution direction. This magnitude of strain, over 6 seconds, would certainly be a measurable effect.

5. CONCLUSION

A poroelastic model that includes the effects of fluid flow and the possibility of exchange between fluid compartments was used in conjunction with finite element modeling to predict the effects of fluid flow on the spatio-temporal patterns of soft-tissue elastic strain under a variety of physiological conditions.

Numerical simulation results suggest that it may be possible to image the interstitial fluid motion in tissues by measuring the corresponding strain rate. Further, they show that the abnormal tumor microvasculature may increase the strain relaxation rate.

In unconfined tests the total dilatation resulting from the tissue relaxation is controlled by the Poisson's ratio difference between incompressible material (*0.5*) and the solid matrix, while in partially confined tests it is controlled by the unconfined to confined lateral area ratio.

6. REFERENCES

Leiderman R., Barbone P.E., Oberai A.A. and Bamber J.C., 2006, "Coupling between elastic strain and interstitial fluid flow: ramifications for poroelastic imaging", *Phys. Med. Biol.* Vol. 56, pp. 6291-6313.

Mow V C, Kuei S C, Lai W M and Armstrong C G, 1980, "Biphasic creep and stress relaxation of articular cartilage in compression: theory and experiments" *J. Biomech. Eng.,* Vol. 102**,** pp**.** 73–84.

Netti P A, Baxter L T, Boucher Y, Skalak R and Jain R K, 1997 "Macro- and microscopic fluid transport in living tissues: application to solid tumors" *AIChE J. Bioeng. Food Nat. Prod.,* Vol. 43, pp. 818–34.

Netti P A, Baxter L T, Boucher Y, Skalak R and Jain R K, 1995, "Time-dependent behavior of interstitial fluid pressure in solid tumors: implications for drug delivery", *Cancer Res.*, Vol. 55**,** pp. 5451–8.

Sarvazyan A P, 2001, *Handbook of Elastic Properties of Solids, Liquids and Gases—vol III: Elastic Properties of Solids: Biological and Organical Materials, Earth and Marine Sciences* ed M Levy, H Bass and R Stern (New York: Academic) chapter 5.